High Resolution Simulation and Characterization of Density-Driven Flow in CO_2 Storage in Saline Aquifers

George S. H. Pau*, John B. Bell, Karsten Pruess, Ann S. Almgren, Michael J. Lijewski, Keni Zhang

Lawrence Berkeley National Laboratory, 1 Cyclotron Road, Berkeley, CA 94720

Abstract

Simulations are routinely used to study the process of carbon dioxide (CO_2) sequestration in saline aquifers. In this paper, we describe the modeling and simulation of the dissolution-diffusion-convection process based on a total velocity splitting formulation for a variable-density incompressible single-phase model. A second-order accurate sequential algorithm, implemented within a block-structured adaptive mesh refinement (AMR) framework, is used to perform high resolution studies of the process. We study both the short term and long term behaviors of the process. It is found that the onset time of convection follows closely the prediction of linear stability analysis. In addition, the CO_2 flux at the top boundary, which gives the rate at which CO_2 gas dissolves into a negatively buoyant aqueous phase, will reach a stabilized state at the space and time scales we are interested in. This flux is found to be proportional to permeability, and independent of porosity and effective diffusivity, indicative of a convection-dominated flow. A 3D simulation further shows that the added degrees of freedom shorten the onset time and increase the magnitude of the stabilized CO_2 flux by about 25%. Finally, our results are found to be comparable to results obtained from TOUGH2-MP.

1. Introduction

Carbon dioxide (CO_2) sequestration involves injecting CO_2 into saline aquifers. While the primary mechanism of securing the CO_2 relies on a leak-proof formation, secondary geochemical mechanisms can play a significant role, especially on geological time scales. At long times, an immiscible CO_2 gas layer will form on top of the brine in the rock formation. Under ambient temperature and pressure conditions in a typical aquifer, CO_2 will dissolve into the brine and increase the density of the brine at the interface of the layers by 0.1-1%, depending on the salinity of the brine [2, 8]. Due to gravitational instability and the heterogeneity in the rock properties of the aquifer, CO_2-rich brine fingers will form, leading to a convective flow that transports these CO_2-rich brines downward while driving brine with low CO_2 concentration upwards. This then accelerates the rate at which CO_2 is dissolved and provides a more secure mechanism by which CO_2 can be stored.

This dissolution-diffusion-convection process has been analyzed in a number of studies. In [2, 3, 9, 11], linear stability analyses yield useful relations on the onset time for convection, dominant wavelength for growth of convective plumes and the growth rates of these fingers. Numerical simulations were also performed to further elucidate the process, and to validate

*Corresponding author. Tel.:+1 510 486 7196; fax: +1 510 486 6900.

Fluid properties	
viscosity, μ	0.5947×10^{-3} Pas
water density, ρ_w	994.56 kgm^{-3}
saturated CO_2 mass fraction, X_1	0.049306
density increase due to CO_2 dissolution, $\Delta\rho$	10.45 kgm^{-3}
diffusivity, $\mathcal{D}$	2×10^{-9} m^{2}s^{-1} [10]

Table 1: Fluid properties.

the linear stability analyses. For example, Riaz *et al.* [9] performed numerical simulation of single-phase Boussinesq-flow and demonstrated that their analysis and the simulation results are consistent. Pruess and Zhang [8] examined long term behavior of the CO_2 flux, in addition to the onset of convection. Their simulation uses a full compressible model with detailed equation of states.

In this work, we perform accurate high-resolution simulations of the process based on a variable-density incompressible model described in Section 2. The problem is formulated so that we can efficiently solve the resulting system of equations using a parallelized second-order accurate block-structured adaptive method described in Section 3; the adaptivity allows us to capture the dynamics of the diffusion-convection process in great details. We then study some numerical aspects of the algorithm before using the method to characterize the diffusion-convection process. In particular, we examine how the onset time of convection and long-term stabilized mass flux vary with permeability, porosity, and effective diffusivity. The analyses are based on a 2D model problem. We finally examine a full 3D problem based on hydrogeologic parameters appropriate for the Carrizo-Wilcox aquifer in Texas [4]. Some of the results are compared to those obtained through TOUGH2-MP, a parallelized version of the general-purpose simulator TOUGH2/ECO2N [6, 7, 12].

2. Problem Formulation

2.1. Setup

Figure 1 shows the simulation setup for a two dimensional problem. The simulation domain, of height H and width W, is impermeable on the top and bottom boundaries and is periodic on left and right boundaries. The CO_2-saturated brine forms a separate layer above the impermeable top boundary; we assume the dissolution rate of CO_2 gas into the layer is sufficiently high that the layer remains saturated for the length of the simulation. We allow diffusion of CO_2-saturated brine into the simulation domain through the top boundary. This simulation setup then allows us to use a variable-density single-phase incompressible model to treat the dissolution-diffusion-convection process.

The fluid properties, as specified in Table 1, are derived from the ECO2N fluid module of TOUGH2 [7] and correspond to pure water (no salinity) at temperature and pressure conditions of $T = 45°$C, $P = 100$ bar, as would be encountered in typical terrestrial crust near 1000 m depth. Isothermal conditions are assumed.

2.2. Governing Equations

The mass conservation equations are given by

$$\frac{\partial \phi \rho X_\alpha}{\partial t} + \nabla \cdot (\rho X_\alpha \mathbf{u}) = \nabla \cdot \phi \tau \mathcal{D} \rho \nabla X_\alpha, \quad \alpha = 1, 2 \tag{1}$$

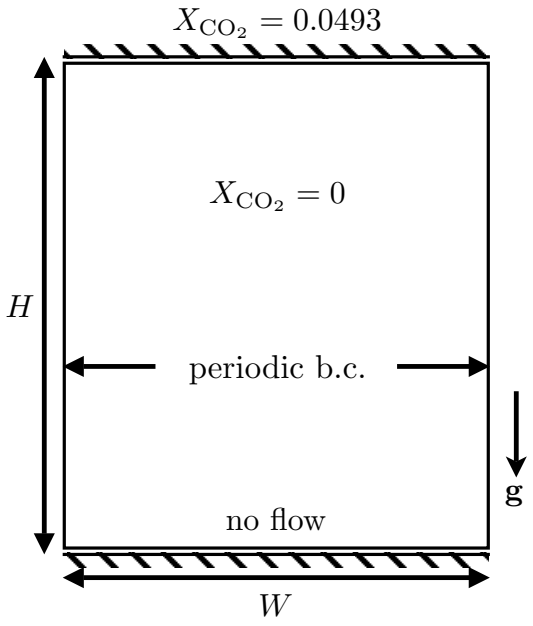

Figure 1: Setup

where X_1 is the mass fraction of CO_2, X_2 is the mass fraction of water, ρ is the density of the aqueous phase, τ is the tortuosity coefficient, $\mathcal{D}$ is the diffusion coefficient, and ϕ is the porosity coefficient. The term $\tau\mathcal{D}$ is also known as the effective diffusivity. The volumetric flux $\mathbf{u}$ is given by Darcy's law:

$$\mathbf{u} = -\frac{\kappa}{\mu}(\nabla p - \rho \mathbf{g}). \tag{2}$$

The system is closed by the equation of state given by

$$\rho\left(\frac{X_1}{\rho_1} + \frac{X_2}{\rho_2}\right) = 1, \tag{3}$$

where ρ_1 is the density of saturated aqueous CO_2 and ρ_2 is the density of water. The equation of state reflects the condition that there is no volume change upon mixing. We note that by summing (1) over all the components, we obtain

$$\frac{\partial \phi\rho}{\partial t} + \nabla \cdot (\rho \mathbf{u}) = 0, \tag{4}$$

For this system, we want to understand how the equation of state constrains its evolution. In particular, we want to relate the equation of state to a condition on the velocity divergence. This will then allow us to derive a pressure equation for use in our IMPES-like sequential scheme described in Section 3. We first define

$$\mathbf{D}_\phi = \phi\frac{\partial}{\partial t} + \mathbf{u}\cdot\nabla, \tag{5}$$

which is a scaled Lagrangian derivative. Then, (1) and (4) can be expressed as

$$\rho\mathbf{D}_\phi X_1 = \nabla\cdot\phi\tau\mathcal{D}\rho\nabla X_1, \tag{6}$$

$$\mathbf{D}_\phi\rho + \rho\nabla\mathbf{u} = 0. \tag{7}$$

If we apply $\mathbf{D}_\phi$ to (3), we obtain

$$\frac{1}{\rho}\mathbf{D}_\phi\rho + \sum_{\alpha=1}^{2}\frac{\rho}{\rho_\alpha}\mathbf{D}_\phi X_\alpha = 0. \tag{8}$$

By substituting (6) and (7) into the above, we obtain

$$\nabla\cdot\mathbf{u} = \sum_{\alpha=1}^{2}\frac{1}{\rho_\alpha}\nabla\cdot\phi\rho\tau\mathcal{D}\nabla X_\alpha. \tag{9}$$

Similar results are obtained in [1].

Substituting (2) into (9), we obtain an elliptic equation given by

$$-\nabla\cdot\frac{\kappa}{\mu}(\nabla p - \rho\mathbf{g}) = \sum_{\alpha=1}^{2}\frac{1}{\rho_i}\nabla\cdot\phi\rho\tau\mathcal{D}\nabla X_\alpha. \tag{10}$$

We impose no flow boundary condition on the bottom boundary; $-\frac{\kappa}{\mu}\nabla p = \sum_{\alpha=1}^{2}\frac{1}{\rho_\alpha}\rho\tau\mathcal{D}\nabla X_\alpha$ on the top boundary; and periodic boundary conditions in all other directions.

Compared to a model with the Boussinesq approximation [9], compositional effects on density are taken into full consideration. Within the incompressible framework, the model presented is exact and does not add much computational cost to a simulation based on a model that employs the Boussinesq approximation. In addition, the use of Boussinesq approximation necessitates the use of either perturbed initial condition [9] or randomized porosity to initiate the instability. With the present model, a random permeability will eventually lead to convective flow, providing a more natural way to analyze the effects of heterogeneity of rock properties.

3. Numerical Method

The basic integration scheme is based on the total velocity approach. Component equations (1) and the pressure equation (10) form a set of coupled equations that can be efficiently solved by an IMPES-type method in which the pressure equation is solved implicitly and the mass conservation equations are solved semi-explicitly. However, we have modified the basic algorithm such that the overall splitting approach is second-order accurate in time and we treat the diffusion terms semi-implicitly so that the diffusive term $\nabla\phi\rho\tau\mathcal{D}\nabla X$ does not limit the time step. We summarize the discretization and time-stepping procedure for a single grid.

The spatial discretization uses a volume of fluid approach in which $(\rho X_\alpha)^n_{ijk}$ denotes the average value of ρX_α over cell (i,j,k) at time t^n; X_α and p are defined on cell centers while $F_\alpha = \rho X_\alpha\mathbf{u}$ and $\mathbf{u}$ are defined on cell edges. The time stepping procedure is then given as follows.

- **Step 1:** Solve the discretized pressure equation (9), given by

$$\mathbf{D}\lambda(\mathbf{G}p) = \mathbf{D}\lambda\rho\mathbf{g} - \mathbf{D}\sum_{\alpha=1}^{2}\frac{1}{\rho_\alpha}\phi\rho\tau\mathcal{D}(\mathbf{G}X_\alpha), \tag{11}$$

for p with properties evaluated using ρ^n and X^n. We then use equation (2) to define the Darcy velocity $\mathbf{u}^n$. Here $\mathbf{D}$ and $\mathbf{G}$ are second-order accurate discretizations of the divergence and gradient operators, respectively. The divergence operator returns a cell-centered divergence from face-centered values; the gradient operator differences cell-centered values to return normal gradients on faces. In two dimensions the discretization of $\mathbf{D}\lambda(\mathbf{G}p)$ at cell (i,j) would be

$$\frac{\lambda_{i+\frac{1}{2},j}(p_{i+1,j}-p_{i,j})-\lambda_{i-\frac{1}{2},j}(p_{i,j}-p_{i-1,j})}{\Delta x}+\frac{\lambda_{i,j+\frac{1}{2}}(p_{i,j+1}-p_{i,j})-\lambda_{i,j-\frac{1}{2}}(p_{i,j}-p_{i,j-1})}{\Delta y}$$

where Δx and Δy are the mesh spacings in the x and y directions, respectively.

- **Step 2:** Use (1) to advance the solution from time t^n to time t^{n+1} based on $\mathbf{u}^n$. We use an unsplit second-order Godunov scheme to compute the hyperbolic fluxes. The Godunov discretization is then coupled to a Crank-Nicolson discretization of the diffusive terms, so that

$$\phi\frac{(\rho X)^{n+1,*}-(\rho X)^n}{\Delta t}+\mathbf{D}F^{n+1/2,*}=\frac{1}{2}\left(\sum_{i=1}^{2}\mathbf{D}\frac{1}{\rho_i^n}\phi\rho^n\tau\mathcal{D}\mathbf{G}X^n+\mathbf{D}\frac{1}{\rho_i^{n+1,*}}\phi\rho^{n+1,*}\tau\mathcal{D}\mathbf{G}X^{n+1,*}\right) \tag{12}$$

  with a suitable linearization of the coefficients of the diffusion term; here superscript $(n+1,*)$ denotes functions of ρX evaluated at $(\rho X)^{n+1,*}$. In this step, $F^{n+1/2,*}$ denotes time-centered fluxes computed using the Godunov procedure but with the total velocity evaluated at t^n.

- **Step 3:** Solve the pressure equation (9), with properties evaluated using $(\rho X)^{n+1,*}$, to compute a new total Darcy velocity $\mathbf{u}^{n+1}$ from (2). We then define $\mathbf{u}^{n+1/2}=1/2(\mathbf{u}^n+\mathbf{u}^{n+1})$ so that we can time center the dependence of the flux on $\mathbf{u}$.

- **Step 4:** Use (1) to re-advance the solution from time t^n to time t^{n+1}, this time using $\mathbf{u}^{n+1/2}$ to obtain values of $(\rho X)^{n+1}$,

$$\phi\frac{(\rho X)^{n+1}-(\rho X)^n}{\Delta t}+\mathbf{D}F^{n+1/2}=\frac{1}{2}\left(\sum_{i=1}^{2}\mathbf{D}\frac{1}{\rho_i^n}\phi\rho^n\tau\mathcal{D}\mathbf{G}X^n+\mathbf{D}\frac{1}{\rho_i^{n+1}}\phi\rho^{n+1}\tau\mathcal{D}\mathbf{G}X^{n+1}\right) \tag{13}$$

  again with a suitable linearization of the coefficients of the diffusion term. In this step, $F^{n+1/2}$ denotes time-centered fluxes computed using the Godunov procedure but with the total velocity evaluated at $t^{n+1/2}$.

The overall time-stepping procedure is integrated into an adaptive mesh refinement (AMR) framework to efficiently accommodate the difference in scale between the diffusive boundary layer and the large-scale convective fingers. Details of the algorithm are described in [5]. Our approach to adaptive refinement uses a nested hierarchy of logically rectangular grids with simultaneous refinement of the grids in both space and time. The grid changes with time based on a set of user-defined refinement criteria; we use component density gradients of all the components. Shown in Figure 2 is a snapshot of the grid; finer grids are placed in regions where small features with large concentration gradients are present. The resulting algorithm is parallelized and shows good scaling behavior up to several thousand CPUs.

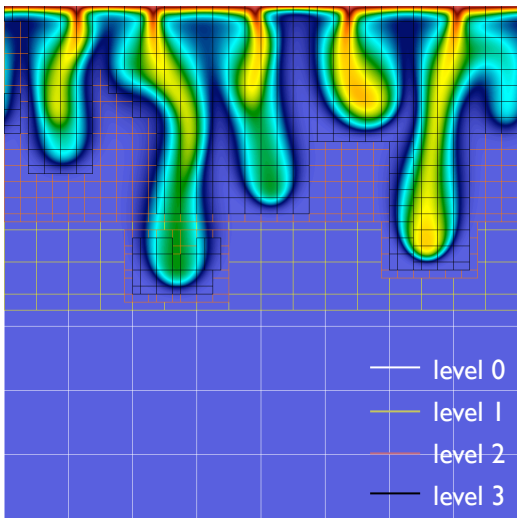

Figure 2: AMR grid with three levels of refinement. Each level of grids is shown with a different color.

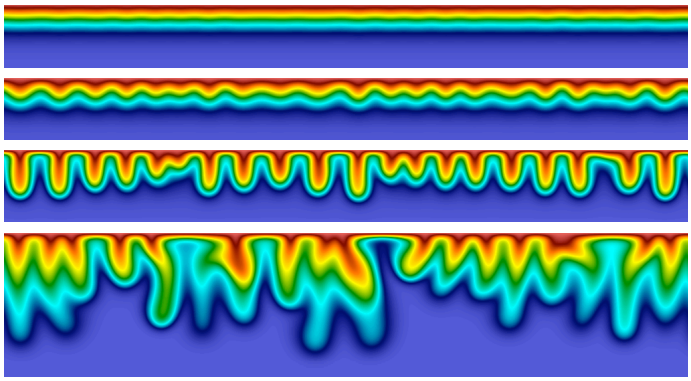

Figure 3: Component density of CO_2(aq); time increases from top to bottom.

4. Results

4.1. Onset of Convection

Figure 3 shows a sequence of snapshots of the density of $CO_{2(aq)}$. They depict the transition from a diffusion-dominated flow to a convection-dominated flow; we note that there is no abrupt change. The slight fluctuations in the diffusive layers, shown in the top snapshot, grow into prominent fingers. These fingers subsequently merge to form larger fingers, developing into a more complex flow pattern. Thus the onset time of convection cannot be defined in an absolute sense. Here, we define onset time of convection, t_{onset} as the time at which the average mass flux at the top boundary, F_0, has a relative deviation of 1% from a pure diffusive mass flux and use this definition to determine the time at which convection becomes an important transport mechanism.

During the initial stage of the flow, we are interested in determining the onset time of convection, and how this is affected by the magnitude of and variability in the permeability, porosity and effective diffusivity. The effects are examined directly by creating permeability or porosity distributions with a random fluctuation about a mean value of $\bar{\kappa}$ or $\bar{\phi}$ respectively. In subsequent sections, magnitudes of the mean properties are given by $\bar{\kappa} = 10$ D, $\bar{\phi} = 0.3$ and $\tau\mathcal{D} = 2 \times 10^{-9}$ m^{2}s^{-1}, except where noted.

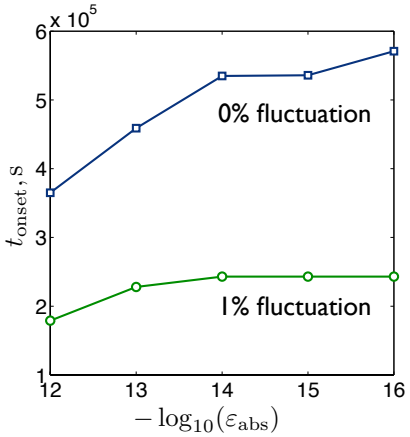

Figure 4: Examining effects of numerical errors on onset time.

4.1.1. Numerical Considerations

We begin this section with an analysis of the influence of numerical errors on the onset time. For homogeneous permeability and porosity, the two-dimensional problem at hand can be essentially reduced to a one-dimensional diffusion problem. Convective transport is only induced when a non-uniform flow field is generated by the heterogeneity in the permeability or the porosity function. However, linear solvers with finite tolerances can introduce small non-uniform errors that can also eventually lead to instability and convective flow. It is imperative that we ensure that any convective transport in our simulation is induced by heterogeneity in formation properties, and not due to finite tolerances of the linear solver we use. In particular, the tolerances must be sufficiently small that they have limited influence on the dynamics of the flow, and thus the onset time.

Since the Darcy velocity is computed from the pressure, we will look at tolerances of the linear solver used to solve the pressure equation in our numerical scheme. Our multigrid linear solver uses two tolerances to control the accuracy of the linear solve: the relative error tolerance, ε_{rel} and the absolute error tolerance, ε_{abs}. Figure 4 shows that with a uniform $\bar{\kappa} = 10$ D and $\varepsilon_{\text{rel}} = 10^{-12}$, numerical errors will indeed lead to an onset of convection. However, the numerically-induced onset time increases with decreasing ε_{abs}, reflecting the decreasing magnitude of the numerical errors. The numerically-induced onset times are more than a factor of 2 larger than the onset times obtained when 1% fluctuation in κ is introduced. Even then, we note that the onset time converges to a value of 2.3×10^5 s only when $\varepsilon_{\text{abs}} \leq 10^{-14}$; numerical errors lead to shorter onset times at tolerance levels of $\varepsilon_{\text{abs}} = 10^{-12}$ and 10^{-13}. Decreasing ε_{rel} to 10^{-14} does not change the results. We thus conclude that the convergence criteria given by $\varepsilon_{\text{rel}} = 10^{-12}$ and $\varepsilon_{\text{abs}} = 10^{-14}$ are sufficient to ensure the onset times determined from our simulations are not adversely affected by numerical errors. The above analysis also shows that our method has excellent control of the numerical errors; with appropriate tolerances, we are able to ensure the numerical errors have negligible effects on our simulation.

Another factor that affects the accuracy of the simulation is the grid resolution. Based on linear stability analysis, the dimensional critical wavelength λ_c is defined as [9]

$$\lambda_c = \frac{2\pi\mu\tau\mathcal{D}}{0.07\kappa\Delta\rho g}. \tag{14}$$

To fully capture the dynamics during the onset of convection, the dimensions of the simula-

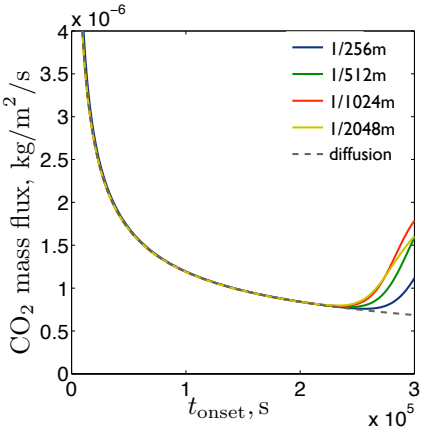

Figure 5: Flux variation at different resolutions. The % fluctuation varies as a function of resolution.

h	% fluctuation	onset time, s
1/256	0.25	2.44×10^5
1/512	0.5	2.33×10^5
1/1024	1	2.26×10^5
1/2048	2	2.23×10^5

Table 2: Onset time for different resolutions. The % fluctuation varies as a function of resolution.

tion domain must be significantly larger than λ_c. For the parameters given in Table 1, λ_c=0.1 m. Thus, our simulation domain, which has a width that is 10 times larger, is adequate.

However, the grid resolution must still be sufficiently high to resolve λ_c so that we can capture the initiation of convective flow accurately. We perform a grid convergence study to determine the appropriate grid size. To ensure the underlying statistics are consistent at different grid resolutions for an uncorrelated random distribution, we adjust the level of fluctuation with grid size. It reflects the notion that for a truly random medium, as grid blocks become larger, the variance of the fluctuations will be lower because of averaging. For example, an initial 1% fluctuation for a given resolution has to be reduced by half when the grid size in each direction is doubled. Experiments confirm that this provides a better convergence behavior.

We examine four grid sizes: $\Delta x = 1/256$, $1/512$, $1/1024$, and $1/2048$. The corresponding fluctuations are given by 0.25%, 0.5%, 1% and 2%. Figure 5 shows that the onset time converges to a single value. From Table 2, we can conclude that the onset time converges to 2.23×10^5s. An effective resolution of $\Delta x = 1/1024$, which is a factor of 100 smaller than λ_c, is thus sufficient. Results in subsequent sections are obtained based on the tolerances and effective resolution established here.

4.1.2. Onset time

Here, we determine how onset time varies with magnitudes of the relative fluctuations in formation properties. We expect onset time to decrease when the magnitude of the fluctuations is increased. This is indeed borne out by Figure 6. However, Figure 6 further shows that for similar levels of % fluctuation, fluctuation in ϕ leads to faster onset time than fluctuations in κ. Furthermore, the rates at which the onset times decrease with increasing fluctuation strength are similar.

Linear stability analysis [2] suggests that the onset time is related to properties of the

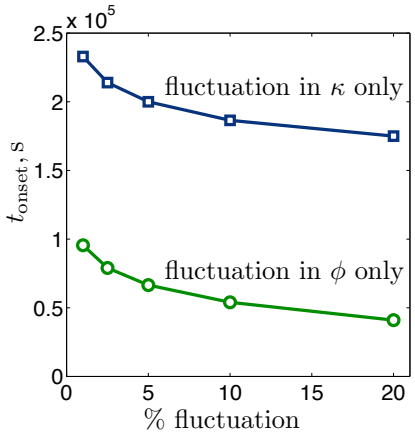

Figure 6: Variation of onset time with % flucutation in ϕ and % fluctuation in κ.

aquifer and fluid through the following relation:

$$t_{\text{onset}} = c_0 \frac{\mu^2 \phi^2 \tau \mathcal{D}}{(\Delta\rho)^2 \mathbf{g}^2 \kappa^2}. \tag{15}$$

We want to determine whether our simulation results can reproduce the relations between t_{onset} and $\bar{\kappa}$, $\bar{\phi}$ and $\tau\mathcal{D}$ in (15). In the κ case, we vary $\bar{\kappa}$ between 0.01 D and 80 D with a 1% level of fluctuation. Similarly, in the ϕ case, we vary $\bar{\phi}$ between 0.05 and 1, again with 1% fluctuation. In the $\tau\mathcal{D}$ case, $\tau\mathcal{D}$ varies from 0.05×10^{-9} m^2s^{-1} to 0.4×10^{-9} m^2s^{-1}. However, $\tau\mathcal{D}$ is uniform and convective behavior is induced by a random κ distribution with a mean of 500 mD and 1% fluctuation with constant $\phi = 0.15$.

Figure 7 clearly shows linear relations between t_{onset} and $1/\bar{\kappa}^2$, $\bar{\phi}^2$, and $\tau\mathcal{D}$ of (15). By determining the gradient of the L_2 fitted line based on the data for κ, we found c_0 to be 3670. However, when the same analysis are performed on the data for ϕ, we found c_0 to be 1796. This again shows that for similar level of fluctuation, fluctuation in ϕ leads to shorter onset time. We can also deduce from Figure 6 that c_0 decreases as the % fluctuation increases.

The magnitude of c_0 is of considerable interest and a wide range of values has been reported in the literature. In most cases, the discrepancies can be attributed to different criteria used to define onset time. In the linear stability analysis performed in [2, 3] that found $c_0 = 75 - 78$, the onset time is determined by minimizing over all possible wavenumbers the time at which the amplification of the square-averaged perturbation is at its minimum. Using the same criterion, Xu *et al.* [11] obtained a similar value for c_0. In Riaz *et al.* [9] that reported a value of approximately 500[1], the onset time is defined as the time at which the growth rate of the amplitude of the dominant mode becomes positive within the linear stability analysis framework. Since we use a different definition of onset time, c_0 values we obtained cannot be directly compared to the values obtained in these studies. However, similar to the current paper, Pruess and Zhang [8] define the onset time based on the deviation of simulated mass flux from a pure diffusive flux, although the % deviation is not specified. They found c_0 to be 1155.6 and 1411.5 for the cases they examined. These

[1]In [9], the onset time relation is given by $t_{\text{onset}} = 146 \frac{\mu^2 \phi \tau \mathcal{D}}{(\Delta\rho)^2 \mathbf{g}^2 \kappa^2}$; the exponent of ϕ is 1 instead of 2. Reinterpreting the results in [9], we deduce $c_0 = 487$ and this is consistent with a separate calculation based on Figure 15 of [9] which gives $c_0 = 506$.

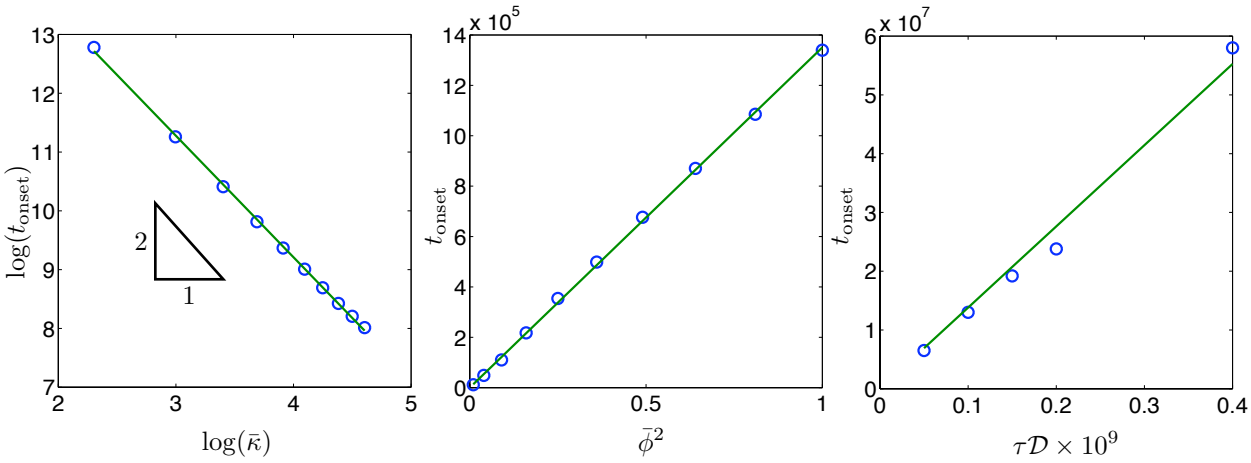

Figure 7: Relations between t_{onset} and $\bar{\kappa}$ (left), $\bar{\phi}$ (center), and $\tau\mathcal{D}$ (right). The circles denote the numerically-determined data and the lines represent best linear-fit. The plots clearly show that t_{onset} is proportional to $1/\bar{\kappa}^2$, $\bar{\phi}^2$ and $\tau\mathcal{D}$.

values are of the same order of magnitude as our reported values; any discrepancy can be attributed to the differences in the actual % deviation used in defining the onset time, the statistics of the underlying heterogeneity in the rock properties, and the equation of states used in the simulations.

4.2. Long Term Behavior

At long time, the flow is characterized by fingers that extend along the length of the domain, as shown in Figure 8. The velocity field shown in the figure shows pockets of circulating flow: the heavier CO_2-rich fluid moves downward in distinct fingers while lighter fluid between the fingers moves upward. However, since the top boundary is impermeable, the upward moving solution must move horizontally, pushing nascent fingers into one another and finally into one of the adjacent extended fingers that has a large downward velocity. This indirectly improves the efficiency by which CO_2 is removed from the top boundary. Within an extended finger, we observe that blobs of aqueous CO_2 with higher concentration may pinch off from the extended finger, and move downward at a greater speed. These blobs eventually diffuse to a point where they are indistinguishable from the extended finger. These observations suggest that the dominant mechanism by which CO_2 is transported downward is through the extended fingers that form after the onset of convection.

In [8], Pruess and Zhang concluded that the resulting CO_2 flux will stabilize to a mean value, and fluctuate with a $\pm 15\%$ deviation from the mean. Accurate characterization of this stabilized flux is important as it allows the dissolution-diffusion-convection process to be modeled as a constant flux in a full-scale carbon sequestration simulation. It also determines the rate at which CO_2 is removed from the highly mobile and buoyant gas phase, and put into a less mobile and negatively buoyant aqueous phase. Thus, the quantification of this rate has important ramifications for storage security. In this section, we will first look at the intricacy of identifying this stabilized flux from numerical simulations. We will then look at how fingering structures vary with κ, ϕ and $\tau\mathcal{D}$. We also determine the empirical relations between the long-time mass flux and these formation properties. Finally, we propose a simple 1D model based on these relations.

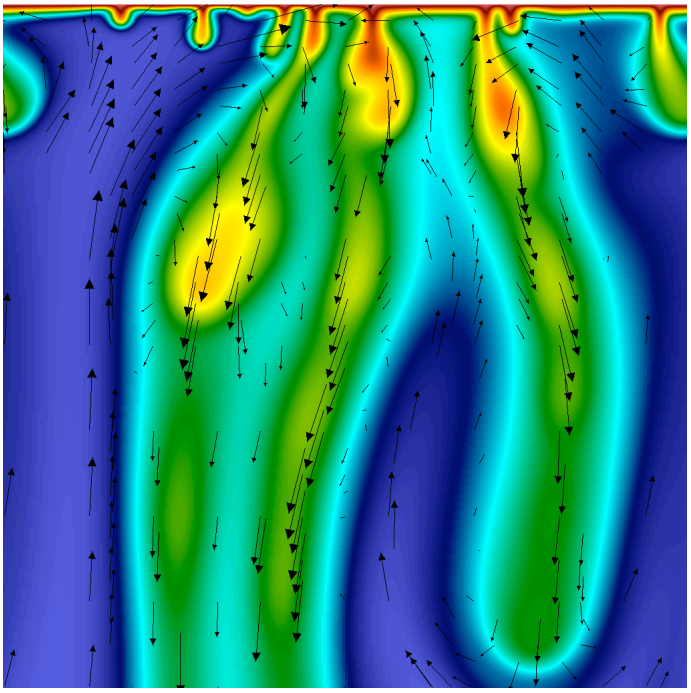

Figure 8: Component density of CO_2(aq) after a long time.

4.2.1. Numerical Considerations

Figure 9 shows the evolution of $F_0(t)$, the mass flux at the top boundary, for a domain of size 1 m $\times$ 8 m. To determine whether the flux has indeed stabilized, we compute the moving average of F_0, defined as

$$F_m(t) = \frac{1}{\Delta t} \int_{t-\Delta t/2}^{t+\Delta t/2} F_0(t')dt' \tag{16}$$

where Δt is sufficiently large that fluctuations in F_m are below 5% for the last N_s time steps at which F_m is evaluated; in this study, $N_s = 100$. We note that in our simulation, the time step is determined based on the advective CFL number which is fixed at 0.75. For different combinations of κ and ϕ, fixed N_s will lead to different values of Δt. A comparison based on fixed N_s (with fixed CFL number) instead of fixed Δt then allows us to take the scale differences in space and time into consideration. We further define the stabilized flux $\langle F_0 \rangle$ as

$$\langle F_0 \rangle = \frac{1}{\Delta T} \int_{T-\Delta T}^{T} F_m(t)dt \tag{17}$$

where T is the last t at which F_m is evaluated, and ΔT is chosen such that the interval $[T - \Delta T, T]$ contains N_s sample points of F_m. The fingers should be sufficiently far from the bottom of the simulation domain at time $T + \Delta t/2$. For this particular case, $\Delta t = 3.1 \times 10^6$s, and $\langle F_0 \rangle$ is found to be 1.46×10^{-6} kg/m^2/s; $F_m(t)$ is also shown in Figure 9.

We note that F_0 fluctuates in excess of 25% with respect to $\langle F_0 \rangle$. This is likely due to boundary effects: the domain, with a width of 1 m, can only accommodate two extended fingers. There are thus insufficient fingers to provide a good averaging for determining $\langle F_0 \rangle$. In Table 3, we increase the width of the domain and determine $\langle F_0 \rangle$, the maximum relative deviations from $\langle F_0 \rangle$ in the sample set used to compute $\langle F_0 \rangle$, and the number of fingers for domains with different widths. The fluctuation decreases with increasing width; the relative

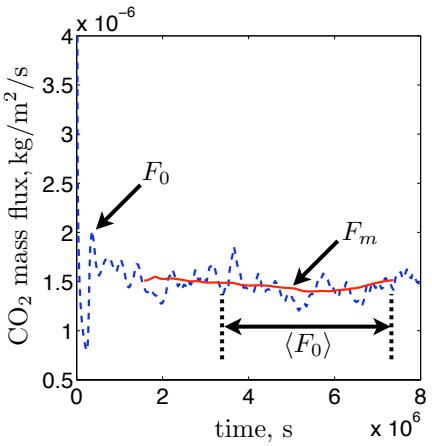

Figure 9: Variation of F_0 and F_m with time. The stabilized mass flux $\langle F_0 \rangle$ is determined based on F_m within the interval indicated in the plot.

W	$\langle F_0 \rangle$, kg/m^2/s	maximum relative deviation	number of fingers
1	1.46×10^{-6}	27.0	2
2	1.48×10^{-6}	12.2	4
8	1.52×10^{-6}	7.2	8
16	1.50×10^{-6}	5.7	17

Table 3: Stabilized mass fluxes for different domain size. The deviation shown is the maximum absolute relative deviation of F_0 from $\langle F_0 \rangle$.

deviation of F_0 from $\langle F_0 \rangle$ for W = 16 m is about a factor of 5 smaller than the relative deviation for W = 1 m. The mean also appears to converge to 1.5×10^{-6} kg/m^2/s. This shows that having a width that can accommodate two fingers may be sufficient, but a larger width will lead to better averaging.

We next examine what effects the magnitude of the relative fluctuation has on the stabilized mass flux. Table 4 shows that there is no distinct correlation between $\langle F_0 \rangle$ and the % fluctuation in κ; κ has a mean of 10 D, and constant $\phi = 0.3$ and $\tau\mathcal{D} = 2 \times 10^{-9}$ m^{2}s^{-1} are used. Furthermore, using the solution for the 0.25% fluctuation case as reference, we see that the deviations of $\langle F_0 \rangle$ for all other cases are within the 5% window that we use to determine $\langle F_0 \rangle$. Thus, we can conclude that $\langle F_0 \rangle$ does not depend on strength of the fluctuations.

4.2.2. Stabilized Mass Flux

The characteristics of the fingering phenomenon are primarily determined by the relative strength between the convective process and the diffusive process. As $\bar{\kappa}$ increases, the Darcy velocity $\mathbf{u}$ increases as well due to (2). The convective term $\nabla \cdot \rho X \mathbf{u}$ is correspondingly

% fluctuation	$\langle F_0 \rangle$, kg/m^2/s	maximum % deviation from the 0.25% case
0.25	1.52×10^{-6}	–
0.5	1.50×10^{-6}	1.9
1	1.59×10^{-6}	4.5
2	1.53×10^{-6}	1.0
10	1.55×10^{-6}	2.1

Table 4: Stabilized mass fluxes for different levels of fluctuation.

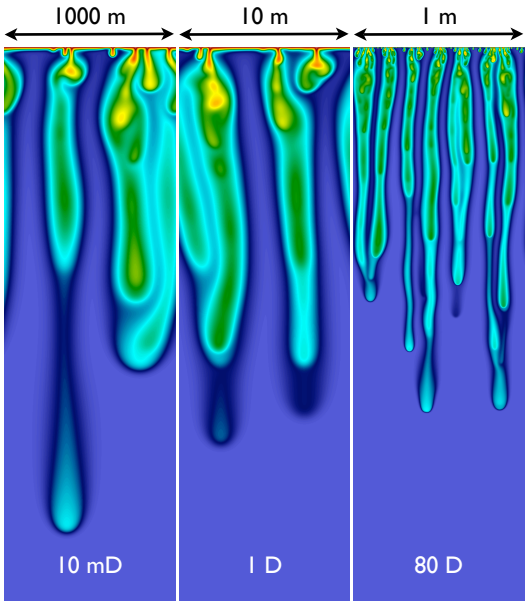

Figure 10: Density of CO_2 for $\bar{\kappa} = 10$ mD, 1 D and 80 D. Time at which the snapshots are taken are respectively 4×10^{12} s, 4×10^{8} s, and 4×10^{5} s.

larger, which diminishes the stabilizing effects of the diffusive process. Thus, more extended fingers are formed per unit width, and these fingers are in general narrower, as shown in Figure 10. On the other hand, an increase in $\bar{\phi}$ reduces the effects of convective process. Thus, as $\bar{\phi}$ increases, the number of fingers per unit width decreases, and the fingers become wider, as shown in Figure 11. Similarly, as $\tau\mathcal{D}$ increases, the number of fingers per unit width decreases, as shown in Figure 12.

Our convergence study in Section 4.2.1 has shown that the long-time mass flux reaches a stabilized state as we approach geological length scales. We would like to determine the empirical relations between $\langle F_0 \rangle$ and various formation properties. To determine these relations, simulations with different combinations of $\bar{\kappa}$, $\bar{\phi}$ and $\mathcal{D}$ are performed. The ranges examined are similar to Section 4.1.2 for most cases. In the κ case, the range is $[0.01, 80]$ D. In the ϕ case, the range is reduced to $[0.05, 0.4]$ because the domain size needed to accommodate sufficient number of fingers for $\phi > 0.4$ can be quite large. Since ϕ is in general small in real aquifers, this smaller range avoids unnecessary demands on the available computational resources. In the $\tau\mathcal{D}$ case, the range we examined is $[0.5, 4] \times 10^{-9}$ $\mathrm{m^2 s^{-1}}$ and κ and ϕ are respectively 500mD and 0.15. Based on Figure 13, we can conclude that $\langle F_0 \rangle$ is proportional to $\bar{\kappa}$ but does not depend on $\bar{\phi}$ and $\tau\mathcal{D}$. This shows that although a decrease in $\bar{\phi}$ or $\tau\mathcal{D}$ leads to an increase in the number of fingers per unit width, it does not imply an increase in $\langle F_0 \rangle$.

These empirical observations suggest that we can model the behavior of the process on geological time and space scales using a simplified model. Let the formation properties be uniform and given by the mean values. Then the mass conservation equation for CO_2 given by (1) can be expressed as

$$\frac{\partial \bar{\phi} \rho X_1}{\partial t} + \nabla \cdot F = \nabla \cdot \bar{\phi} \tau \mathcal{D} \rho \nabla X_1, \tag{18}$$

where $F = \rho X_1 \mathbf{u}$ and $\mathbf{u} = \frac{\bar{\kappa}}{\mu}(\nabla p - \rho \mathbf{g})$. The linear relation between $\langle F_0 \rangle$ and $\bar{\kappa}$ suggests that the dominant mechanism by which CO_2 is transported downward is convective in nature and

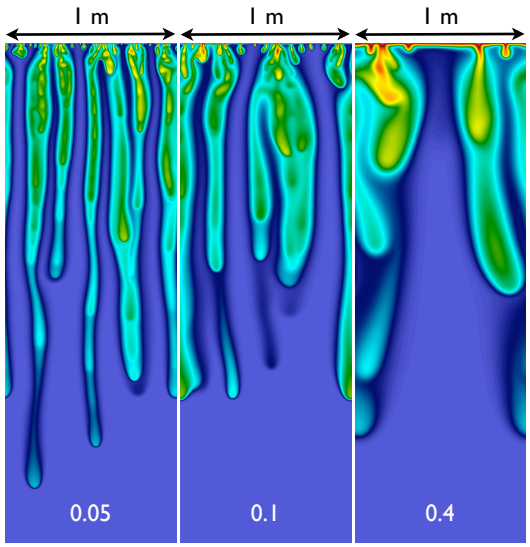

Figure 11: Density of CO_2 for $\bar{\phi} = 0.05$, 0.1 and 0.4. Times at which the snapshots are taken are respectively 6×10^5 s, 1×10^6 s and 6×10^6 s.

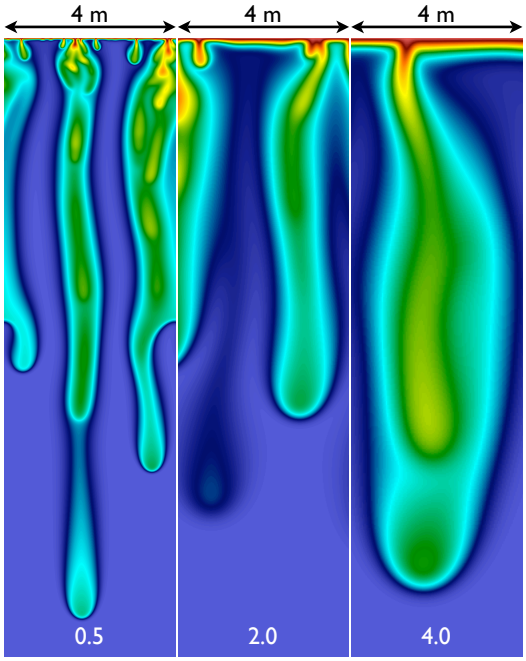

Figure 12: Density of CO_2 for $\tau\mathcal{D} = 0.5$, 1 and 4 $\times 10^{-9}$ $m^2 s^{-1}$. Times at which the snapshots are taken are respectively 2.0×10^8 s, 2.1×10^8 s and 2.6×10^8 s. Note that the solutions for the last two cases are simulated on larger domains but truncated here for comparison.

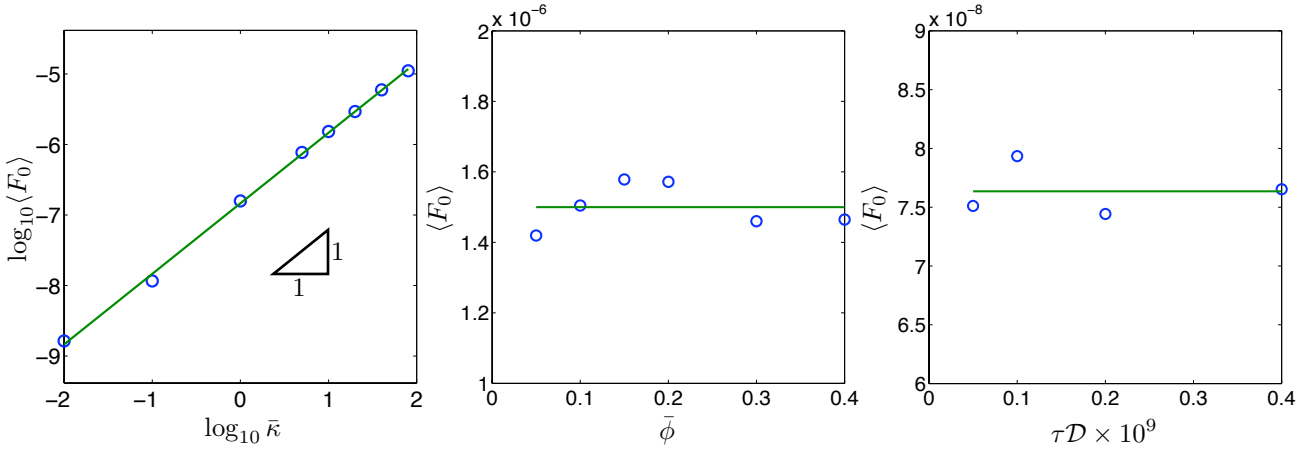

Figure 13: Variation of $\langle F_0 \rangle$ with $\bar{\kappa}$, $\bar{\phi}$ and $\tau\mathcal{D}$.

can be efficiently modeled using the mean values of κ and ϕ. In addition, since $\langle F_0 \rangle$ does not depend on $\tau\mathcal{D}$, we can further approximate the divergence condition (9) by

$$\nabla \cdot \mathbf{u} = 0. \tag{19}$$

Since the top boundary is impermeable, we must model the influx of $CO_{2(aq)}$ at the top boundary explicitly by imposing the boundary condition

$$\bar{\phi}\tau\mathcal{D}\rho\nabla X_1 = \langle F_0 \rangle, \tag{20}$$

at the top boundary, with a corresponding condition for $\bar{\phi}\tau\mathcal{D}\rho\nabla X_2$ so that the net mass flux is zero.

The divergence condition (19), the conservation equation (18) and the boundary condition (20) then constitute a simplified model that is relevant on geological scales where the complex convective pattern at small scales can be approximated by a uniform convective flux. Since the model depends only on the mean values of κ, ϕ, and $\tau\mathcal{D}$, we can avoid the need to resolve the fluctuations that lead to the fingering phenomenon. Thus, we do not need to take the diffusive layer, which is small relative to the geological length scale, and the onset time, which is again small relative to the geological time scale, into consideration. When used as a subgrid model, this model can potentially simplify the inclusion of the dissolution-diffusion-convection process in a large- scale flow simulation of carbon sequestration.

4.3. Three-Dimensional Problem

Here, we perform a full 3D simulation of the diffusion-convection process to determine whether the results will differ significantly from a 2D simulation. Since a 3D simulation is significantly more resource intensive, we will examine only one set of hydrogeologic parameters, corresponding to the Carrizo-Wilcox aquifer in Texas; its deeper sections are very large and promising targets for CO_2 storage [4]. The Carrizo-Wilcox aquifer is modeled as having a mean permeability of 500 mD, a uniform porosity of 0.15 and uniform effective diffusivity of 2×10^{-9} m^2/s; the permeability variation was modeled with a uniform random fluctuation of 1%. The simulation was performed with a parallel implementation of the AMR algorithm in 3D. The domain is of size 8 m $\times$ 8 m $\times$ 32 m. Four levels of grids are used, and grids at the finest level have a resolution of 1/128 m. CPU, memory and storage requirements for

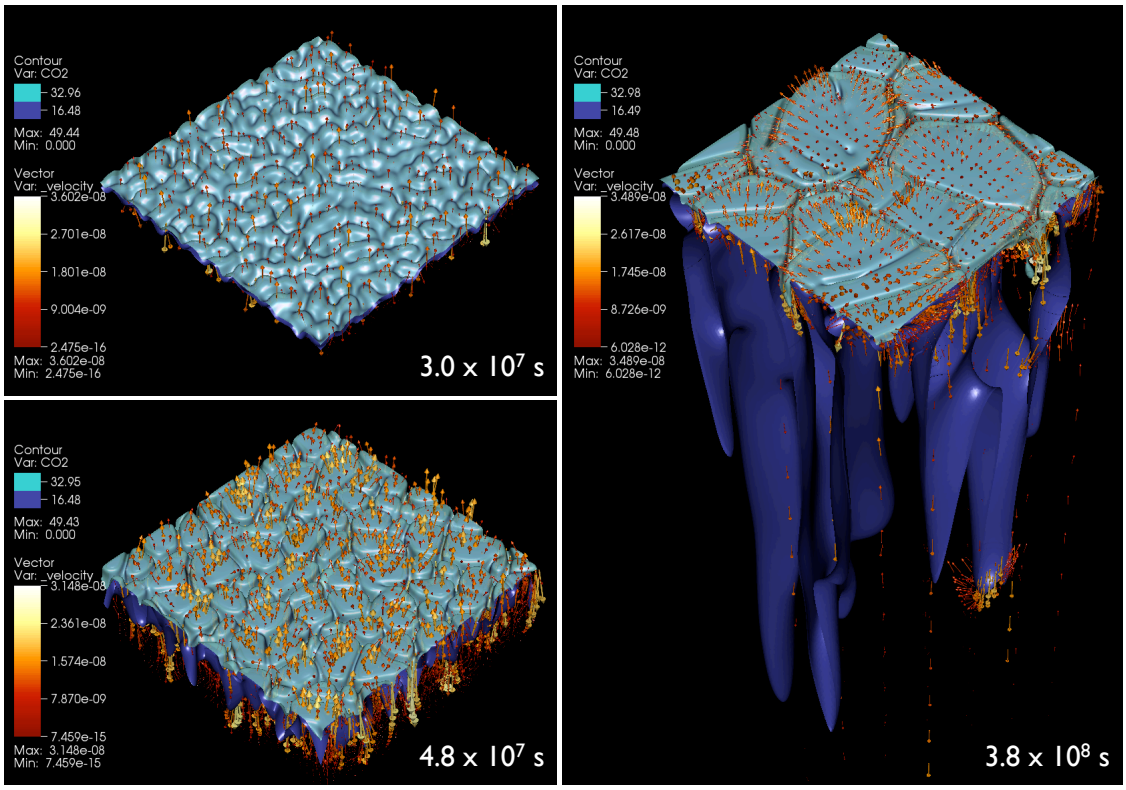

Figure 14: Evolution of the velocity fields and CO_2 densities at different times.

a simulation based on a uniform grid at the finest resolution would have been significantly larger than that required by an AMR-based method.

Figure 14 shows the velocity fields and the contour plots of the CO_2 densities for $t = 3 \times 10^7$ s, 4.8×10^7 s and 3.8×10^8 s. We observe a circulating flow field, similar to 2D results shown in Figure 8. However, when pockets of upward moving fluid reach the top boundary, they move outward in all directions in the horizontal plane. As different pockets of these diverted fluid meet, they form ridges that act as conduits for downward moving fluid; we note that the downward velocity is usually largest along the ridges. At early times, the number of upward moving pockets are numerous but as time progresses, they coalesce to form larger pockets. They eventually reach a pseudo-stabilized state where the maximum size of the pockets stays approximately constant, but the flow pattern still evolves dynamically. In Figure 15, we look at the fingering structure at $t = 3 \times 10^7$ s, 4.8×10^7 s and 3.8×10^8 s: we observe a cellular-like network of nascent fingers that leads to flattened extended fingers. Shown in Figure 15 is also the grid at the finest level.

It is clear from the above that the additional degrees of freedom add significant complexity to the fingering phenomena. We would like to determine whether it has any appreciable influence on the integral measures that we are interested in. In Figure 16, we compare the evolution of F_0 of a 3D simulation to a 2D simulation with the same fluid and formation parameters, and grid resolution. We obtain a somewhat smaller onset time and a higher maximum mass flux during the transient stage. The surge in the CO_2 mass flux is also reflected in Figure 14 where there is a surge in the downward moving fluid at time $t = 3.8 \times 10^7$ s. The fluctuation of mass flux at long time is also smaller compared to the 2D simulation due to larger number of fingers which leads to better averaging. The stabilized mass flux is found

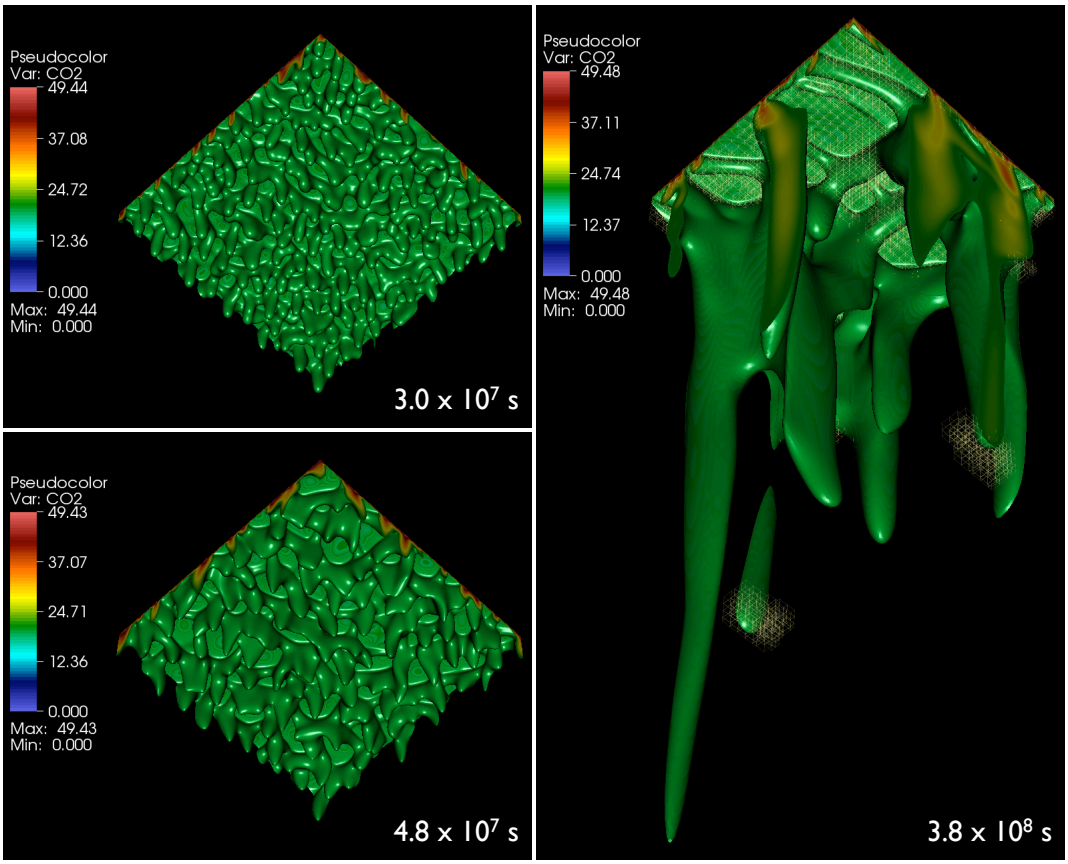

Figure 15: A view from below shows flat characteristic of the fingers. The surface corresponds to a concentration of 20 kg/m^3. The grids shown in the rightmost figure is at the finest level.

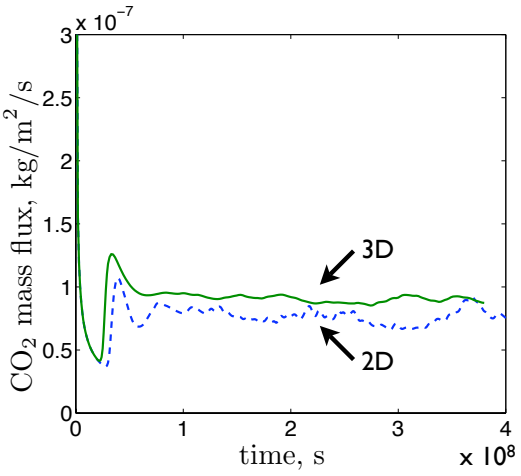

Figure 16: Comparing the results from a 2D simulation and a 3D simulation.

to be 8.97×10^{-7} kg/m^2/s, which is 25% higher than a comparable 2D simulation. While the difference is statistically significant, the increase is small in view of the typically large variation in permeability for geologic media. Thus the effect of additional spatial degrees of freedom on onset time and stabilized mass flux is modest.

5. Comparison to Results from TOUGH2-MP

The same problem of convective instability discussed above was simulated with a parallelized version TOUGH2-MP [12] of the general-purpose reservoir simulator TOUGH2. Initial calculations used the ECO2N fluid property module [7]. However, since the conditions in the present problem are limited to a single aqueous phase, a more efficient simulation can be obtained by using EOS7, in which the fluid is represented as a two-component mixture of H_2O and brine. We use the brine component to represent density changes in the aqueous phase from CO_2 dissolution. Numerical work is approximately proportional to NEQ^2, where NEQ is the number of equations per grid block. Accordingly, a given problem can be solved with EOS7 (NEQ = 2) in less than half the time required with ECO2N (NEQ = 3). Our test calculations have confirmed excellent agreement between simulations using EOS7 and ECO2N.

To achieve results with "small" space discretization errors, we experimented with different domain sizes and grid resolutions. We found a domain of width W = 1 m, height H = 5 m, and a vertical grid resolution of 1 mm near the top boundary, which was gradually coarsened going downward, to be sufficient. Horizontal grid resolution was 10 mm, and the total number of grid blocks was 52,300.[2]

5.1. Results

The convective pattern shows similar features to those seen in the adaptive grid simulations discussed previously, including fingering convection, merging and pinch-off of fingers,

[2]Simulations presented here were performed on a Dell T5400 dual quad core computer with a total of 8 cores, and in most cases 16 processes were run (two per processor), as this was found to reduce total execution time compared to running 8 processes. Depending on grid resolution and simulation time, individual runs typically took from 1/2 to 4 hours.

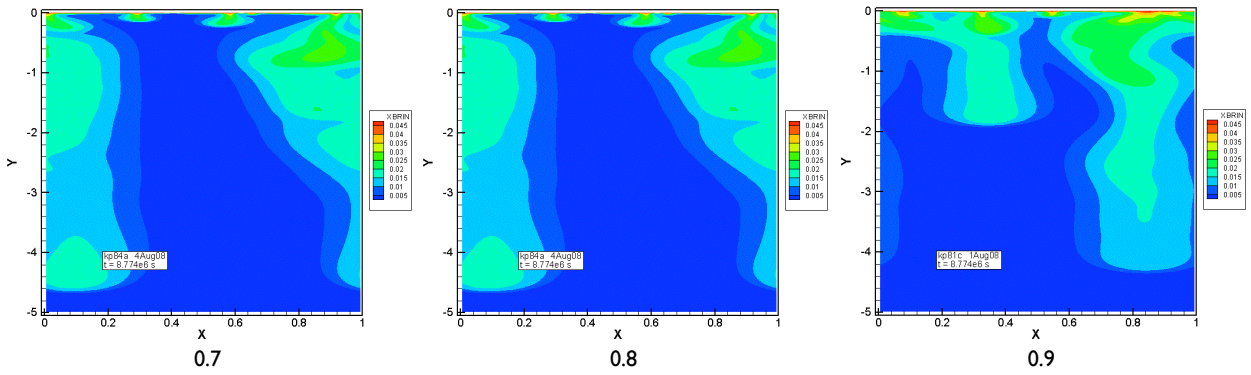

Figure 17: Simulated distribution of dissolved CO_2 after 101.6 days for three different random number seeds to generate permeability heterogeneity (given at the bottom of each plot). Note the different horizontal and vertical scales.

and continuous generation of new fingers as older ones grow. As an example, Figure 17 shows convective patterns for three different random number seeds after a time of 101.6 days. The resolution of features is somewhat inferior in comparison to the adaptive gridding, Figure 8. Specifics of the convective activity are very sensitive to small problem variations, but we observe that integral measures of the process, such as onset time of convection, and long-term behavior of the CO_2 mass flux carried by the convection, are quite robust to modest changes in problem parameters. Indeed, for the three cases with different random permeability fields shown in Figure 17, onset times of convection are identical, and long-term stabilized fluxes show random fluctuations of $\pm$ 15% about the same mean of approximately 1.3×10^{-6} kg/m^2/s.

We explored the sensitivity of the onset time for convection to the random perturbations applied to the medium. Figure 18 shows that the onset time for convection decreases with increasing strength of the applied perturbation of the medium. Porosity perturbations are seen to be more effective in triggering convective instability than permeability perturbations. These results are consistent with the results in Section 4.1.2, as shown in Figure 6.

A comparison calculation with a perfectly homogeneous medium yields a substantially larger onset time, as in this case convective instability arises only from numerical roundoff. The onset times obtained from TOUGH2-MP simulations are around $6 - 9 \times 10^4$ s, about a factor 3 smaller than obtained with the adaptive algorithm. At a nominal onset time of 7.5×10^3 s, the thickness of the diffusive boundary layer is 12.2 mm, which should be well resolved with our 1 mm grid resolution. Potential reasons for the discrepancy are similar to the reasons given for the discrepancy in c_0 discussed in Section 4.1.2.

The convective CO_2 flux at the top is equal to the CO_2 dissolution rate per unit area. Due to the partially chaotic nature of the convection process, this rate fluctuates, but the fluctuations are modest in size, and fluxes stabilize at 1.3×10^{-6} kg/m^2/s ($\pm$ 15%), regardless of how the instability was triggered (Figure 19). This is approximately 13% smaller than the value obtained from the adaptive gridding simulations. This is likely due to the higher resolution achieved by the adaptive gridding simulations, which allow fine-scale convective behavior, including those away from the top boundary, to be resolved.

We also performed simulations with different boundary conditions at the sides and bottom of the domain, such as no flow conditions on the sides, and constant pressure conditions on the bottom. Onset times for convection and long-term stabilized fluxes were found to be

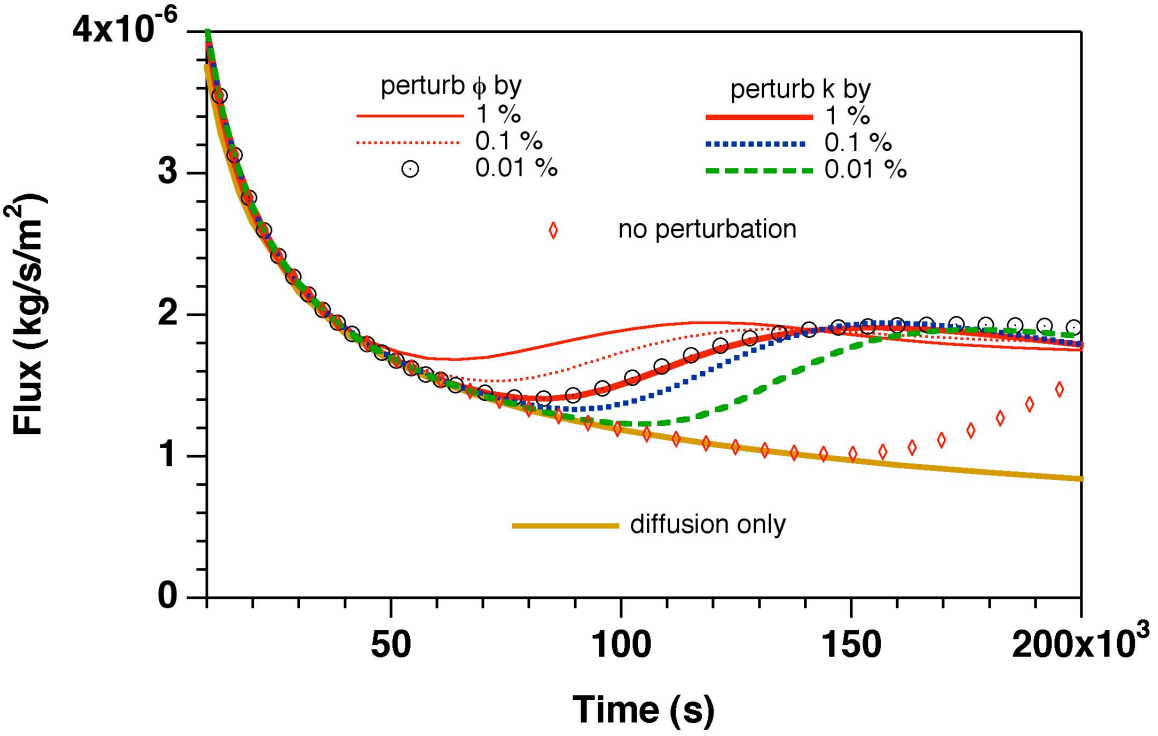

Figure 18: Simulated CO_2 fluxes at the top boundary at early times, for different random perturbations of the porosity or permeability field.

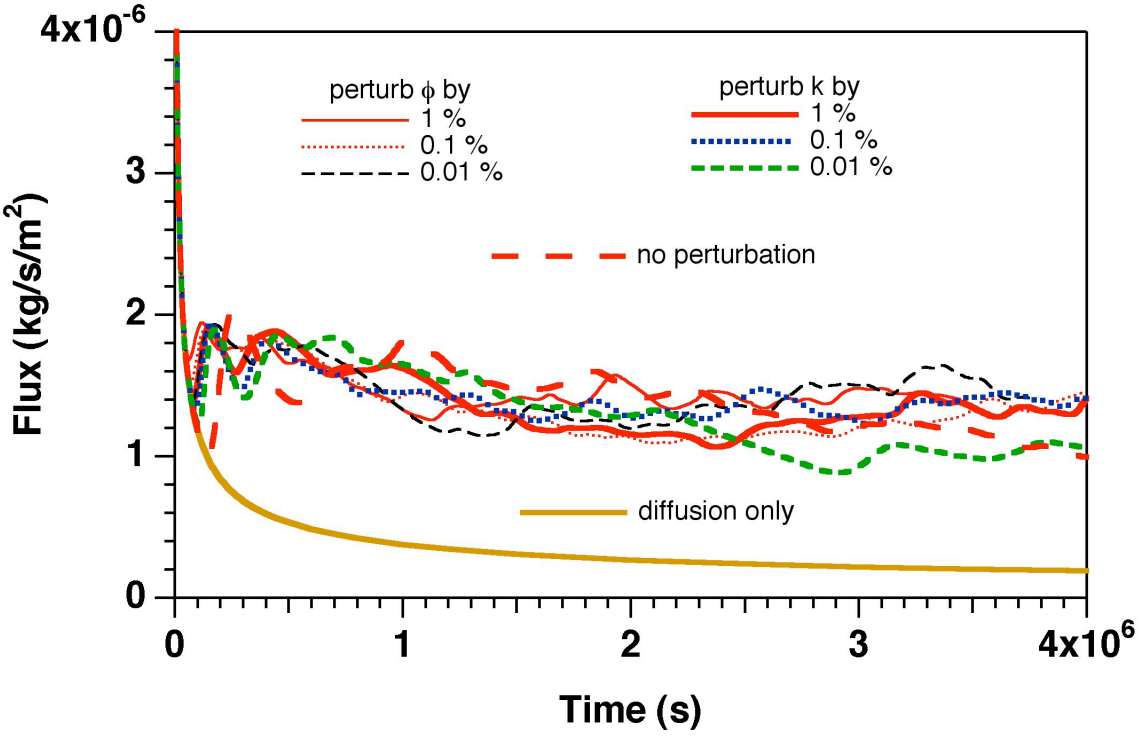

Figure 19: Longer-term behavior of simulated CO_2 fluxes at the top boundary.

insensitive to boundary conditions. A more extensive account of TOUGH2 analyses of the dissolution-diffusion-convection process is available in a laboratory report [8].

6. Conclusion

High-resolution two-dimensional simulations of the diffusion-convection process in CO_2 sequestration were performed using a block structured adaptive mesh refinement method. Numerical aspects of the simulations were examined and the short and long term behaviors of the process are examined.

We found that although details of the convection process are chaotic in nature, integral measures, such as onset time for convection, and long-term CO_2 mass flux associated with the convective activity, are robust and insensitive to modest problem variations. At short time, the onset time of convection follows the prediction of linear stability analysis. The constant c_0 in (15) for onset time is found to be in the range of 1000-5000 and is dependent on the level of fluctuation in the formation properties. It is of the same order of magnitude as that reported in [8] and any discrepancy can be attributed to differences in the details of the simulation parameters. There are however large variations in the value of c_0 reported in the literature. These variations can usually be attributed to differences in the models used to describe the diffusion-convection process, the criteria by which the onset time is determined, and the levels or forms of fluctuations used in the simulations.

At long time, the CO_2 mass flux reaches a stabilized state that approaches a constant value at space and time scales of interest for geological storage of CO_2. In particular, we show that long term behavior is convection-dominated and depends only on the mean value of permeability. It also does not depend on the level of fluctuations. This allows us to propose a simple model that efficiently captures the diffusion-convection process at the geological scales. The model depends only on the mean values of formation properties; we can thus avoid the need to resolve the fluctuations that lead to the fingering phenomena. The use of this model as a subgrid model in a large-scale multiphase flow simulation of carbon sequestration will be examined in future work.

A detailed three-dimensional simulation shows that the added degrees of freedom add significant complexity to the fingering phenomena. However, the changes in the integral measures, i.e. the onset time and stabilized mass flux, are modest when compared to the two-dimensional simulations. Results from the two- dimensional simulations are also compared to results from TOUGH2-MP and good agreement is obtained.

7. Acknowledgement

Support for this work was provided by the Applied Mathematics Research Program and the Office of Basic Energy Sciences of the U.S. Department of Energy under contract DE-AC02-05CH11231. This research used resources of the National Energy Research Scientific Computing Center and the Lawrencium computational cluster resource provided by the LBNL's IT Division, both of which are supported by the Office of Science of the U.S. Department of Energy under the same contract.

References

[1] J. Douglas Jr., D. Frías, N. Henderson, and F. Pereira. Simulation of single-phase multicomponent flow problems in gas reservoirs by Eulerian-Lagrangian techniques. *Transport in Porous Media*, 50:307–342, 2002.

[2] J. P. Ennis-King and L. Paterson. Role of convective mixing in the long-term storage of carbon dioxide in deep saline formations. *SPE J.*, 10(3):349–356, 2005. SPE-84344-PA.

[3] J. P. Ennis-King, I. Preston, and L. Paterson. Onset of convection in anisotropic porous media subject to a rapid change in boundary conditions. *Physics of Fluids*, 17(8):084107, 2005.

[4] J. P. Nicot. Evaluation of large-scale CO_2 storage on fresh-water sections of aquifers: An example from the Texas gulf coast basin. *Int. J. Greenhouse Gas Control*, 2:583–593, 2008.

[5] G. S. H. Pau, A. S. Almgren, J. B. Bell, and M. J. Lijewski. A parallel second-order adaptive mesh algorithm for incompressible flow in porous media. *Phil. Trans. R. Soc. A*, 2009. To be published.

[6] K. Pruess. The TOUGH codes – a family of simulation tools for multiphase flow and transport processes in permeable media. *Vadose Zone J.*, 3:738–746, 2004.

[7] K. Pruess and N. Spycher. ECO2N – a fluid property module for the TOUGH2 code for studies of CO_2 storage in saline aquifers. *Energy Conversion and Management*, 48(6):1761–1767, 2007.

[8] K. Pruess and K. Zhang. Numerical modeling studies of the dissolution-diffusion-convection process during CO_2 storage in saline aquifers. Technical Report LBNL-1243E, Lawrence Berkeley National Laboratory, Calif., 2008.

[9] A. Riaz, M. Hesse, H. A. Tchelepi, and F. M. Orr. Onset of convection in a gravitationally unstable diffusive boundary layer in porous media. *Journal of Fluid Mechanics*, 548:87–111, Feb. 2006.

[10] F. Tewes and F. Boury. Formation and rheological properties of the supercritical CO_2-water pure interface. *J. Phys. Chem. B*, 109(9):3990–3997, 2005.

[11] X. Xu, S. Chen, and D. Zhang. Convective stability analysis of the long-term storage of carbon dioxide in deep saline aquifers. *Advances in Water Resources*, 29(3):397 – 407, 2006.

[12] K. Zhang, Y. Wu, and K. Pruess. User's guide for TOUGH2-MP – a massively parallel version of the TOUGH2 code. Technical Report LBNL-315E, Lawrence Berkeley National Laboratory, Calif., 2008.